Supporting Information

Connecting Deep Aquifer Recharge in California's Central Valley to Sierra Nevada Snowmelt via Multi-Sensor Remote Sensing Data

S. Werth[1], M. Shirzaei[1,2,3], G. Carlson[1,4], and Roland Bürgmann[5]

[1]Virginia Tech, Department of Geosciences, Blacksburg, VA, USA.
[2]Virginia Tech, National Security Institute, Blacksburg, VA, USA.
[3]United Nations University, Institute for Water, Environment and Health, Hamilton, ON L8P 0A1, Canada
[4]University of California, Berkeley, Department of Environmental Science, Policy, and Management, Berkeley , CA, USA
[5]University of California, Berkeley, Department of Earth and Planetary Science, Berkeley, CA, USA.

Correspondence to: Susanna Werth (swerth@vt.edu)

Contents of this file

Introduction

This supplemental material contains additional information in the form of text and figures about deformation in unconfined aquifers due to groundwater level change and Figures with further details about meteorological, GNSS, and GWL data, as well as uncertainty analyses, which are discussed in the main text.

Text S1. Poroelastic Deformation of Unconfined Aquifers

Poroelastic deformation in unconfined aquifers due to changes in groundwater levels exists, but it is much smaller and below a measurable amplitude compared to confined aquifers. Water in unconfined aquifers is released from drainage but not from aquifer compaction or water expansion, as it is in confined aquifers.

To test if the shallower units may contribute significantly to the elastic subsidence, we calculate the subsidence signal related to water level decrease in shallow unconfined aquifers, using the 1-D consolidation model of Terzaghi (detailed in Ojha et al., 2018). The aquifer compaction (db) is given by:

$$db = \frac{b \times \alpha_B \times \rho_w \times g \times dh}{E}$$

where b is the thickness of the shallow aquifer that is recharged due to precipitation, we generously assume it to be 10 m (which is an upper bound and usually is less than a few meters), ρ_w is water density, g is the gravitation acceleration, dh is change in water table due to discharge, which we assume to be also 10 m, namely the entire aquifer is emptied, E is the static bulk modules, which we assume to be 150 MPa after Ojha (2018). α_B is the Biot-Willis coefficient, defined as the ratio of volume of fluid that is added to the aquifer divided by the change in the bulk volume under constant pore pressure, which ranges between 0 (unconfined) and 1 (confined). We set the Biot-Willis coefficient to be 0.2 for the shallow sandy-clay layers in the San Joaquin Valley. The value of elastic subsidence, db, is 1 mm. This value is below the uncertainty of InSAR and GNSS measurements used in here, and thus, we conclude the observed elastic subsidence cannot be due to water level decreases in shallow unconfined aquifers.

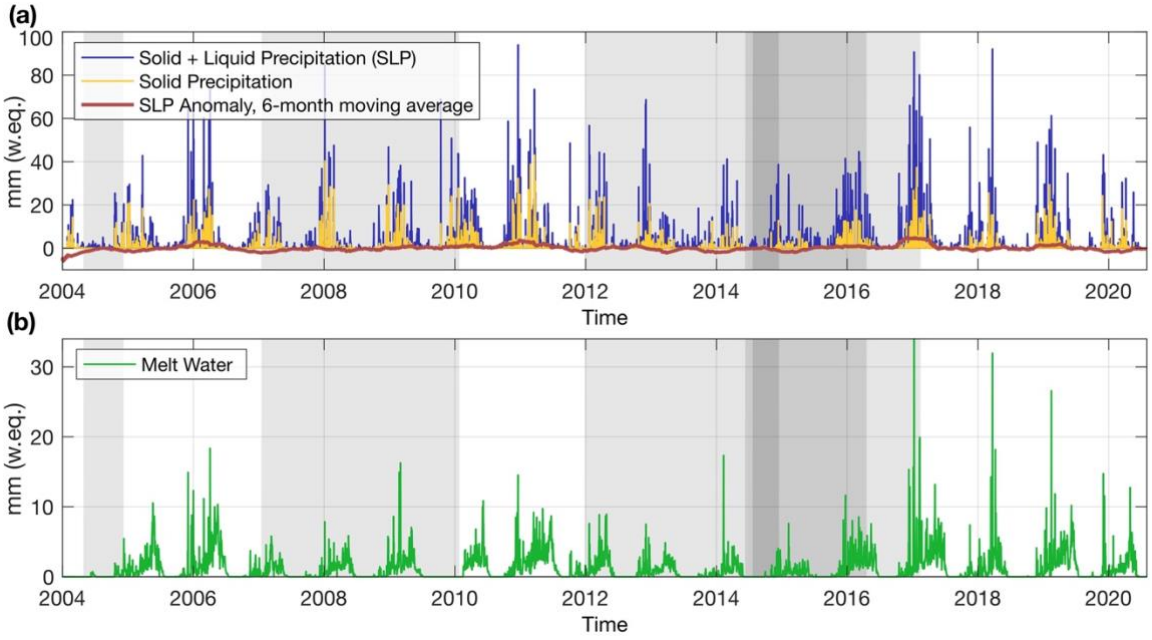

Figure S1. Precipitation and meltwater in the Sierra Nevada recharge area. (a) Daily time series of precipitation in the Sierra Nevada drainage area (rose shaded area in Fig. 1a) as retrieved from the SNODAS dataset. Shown is the sum of liquid and solid precipitation (blue), solid precipitation (yellow), and a 6-months moving average of monthly precipitation anomalies, which were estimated as difference between daily (liquid and solid) precipitation to average precipitation for a respective calendar day during the observation period 01/2004-07/2020. (b) Daily time series of SNODAS meltwater (green) for the same area. Gray shaded background areas (light, medium, dark gray) indicate that the USDM identifies >30% (>30%, >60%) of California's area to be in moderate (exceptional, exceptional) dry condition (compare Fig. S3).

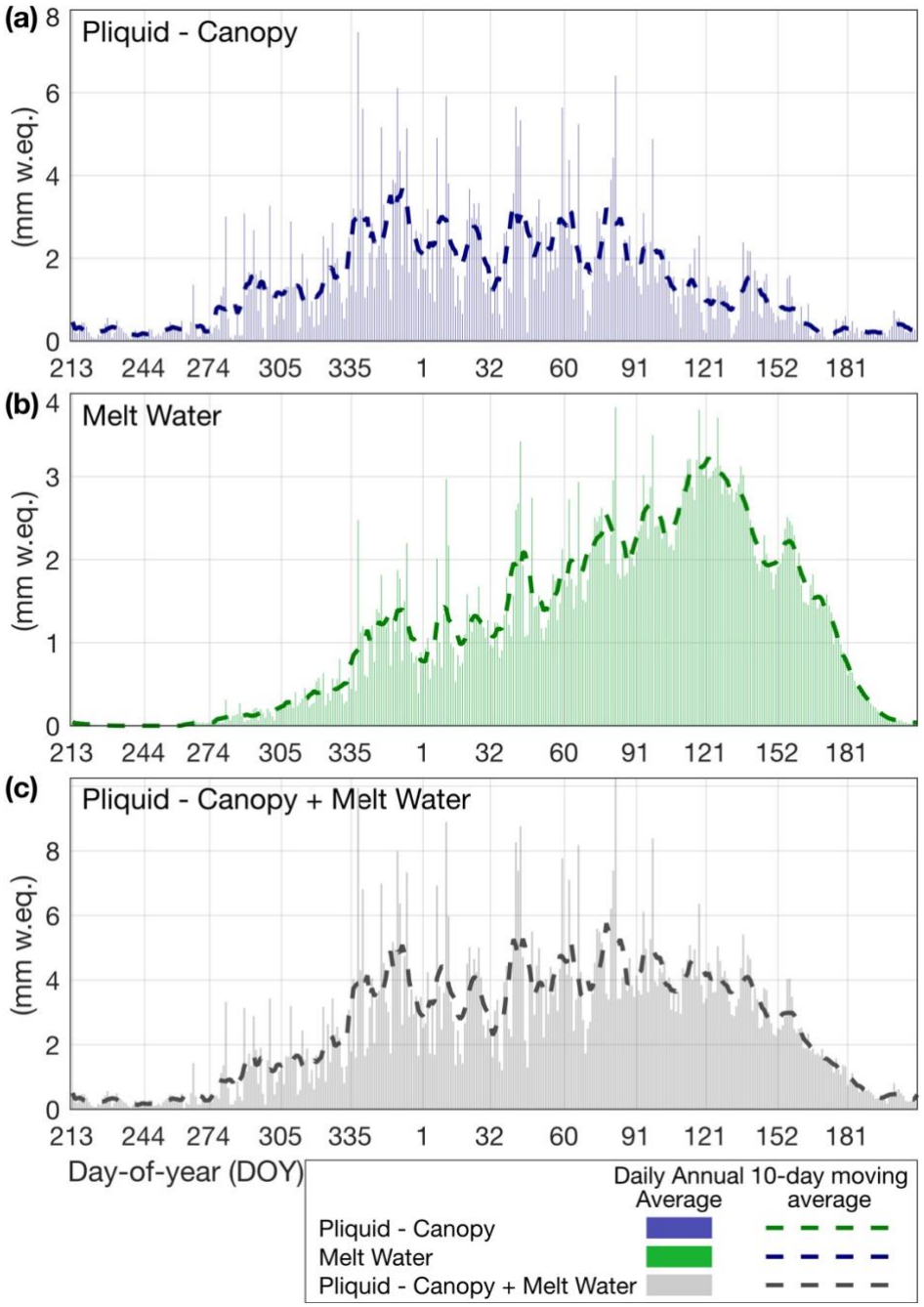

Figure S2. Water availability in the Sierra Nevada. Components of daily annual average water availability in the Sierra Nevada drainage area (rose shaded area in Fig. 1A), which were estimated as difference between daily SNODAS values and average values for a respective calendar day during the observation period 01/2004-07/2020. Values are shown as daily bars for (A) liquid precipitation corrected for canopy interception (20% of liquid precipitation), (B) meltwater, and (C) sum of liquid precipitation corrected for canopy interception plus meltwater. Dashed graphs show 10-day moving average of the respective bar graphs.

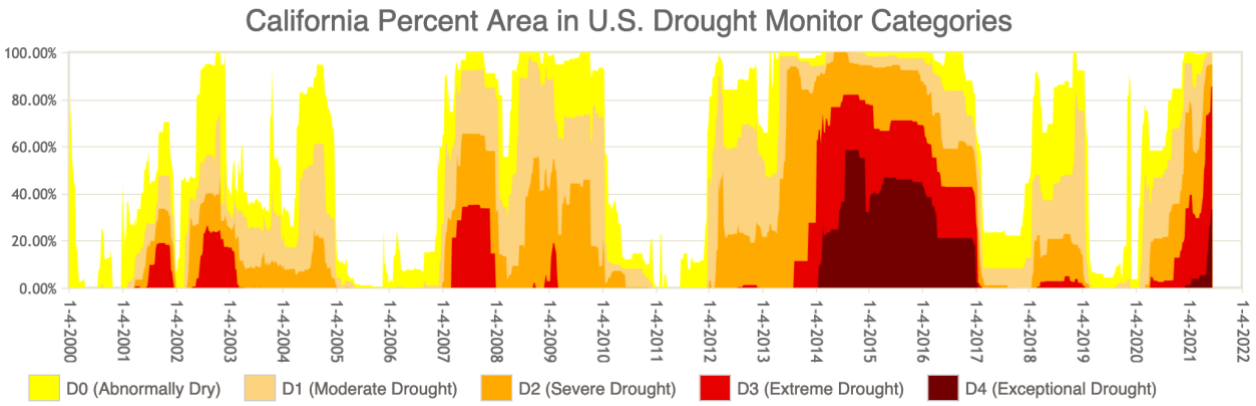

Figure S3. United States Drought Monitor for California. Temporal progression of drought severity in California, during 2000-2022, indicated a percentage of the state's area that experiences a certain drought severity. Different drought severity is indicated by different colors. The time series data were provided by the United States Drought Monitor (USDM) and retrieved from https://droughtmonitor.unl.edu. The U.S. Drought Monitor is jointly produced by the National Drought Mitigation Center at the University of Nebraska-Lincoln, the United States Department of Agriculture, and the National Oceanic and Atmospheric Administration. Map courtesy of NDMC.

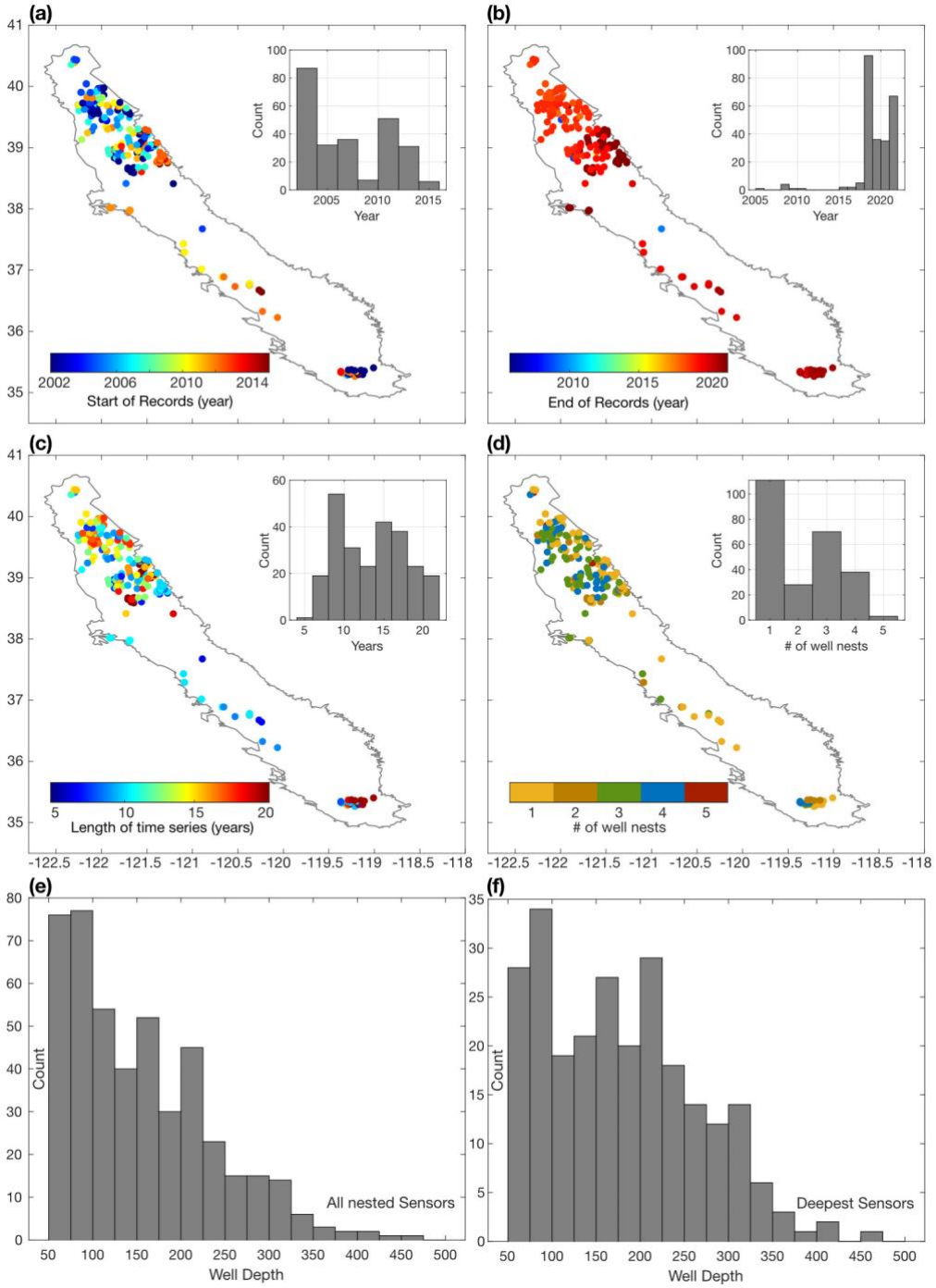

Figure S4. Groundwater well data. Availability of DWR and USGS groundwater level records at well sites with deepest sensor at depth of below 50 m throughout the Central Valley and corresponding histogram: (a) start year of records, (b) end year of records, (c) length of records in years, and (d) number of nested sensors at each observation well. (e) Histogram for number of sensors per depth, including all nested sensors (see d). (f) Histogram for number of sensors per depth only, including deepest sensor at any given site.

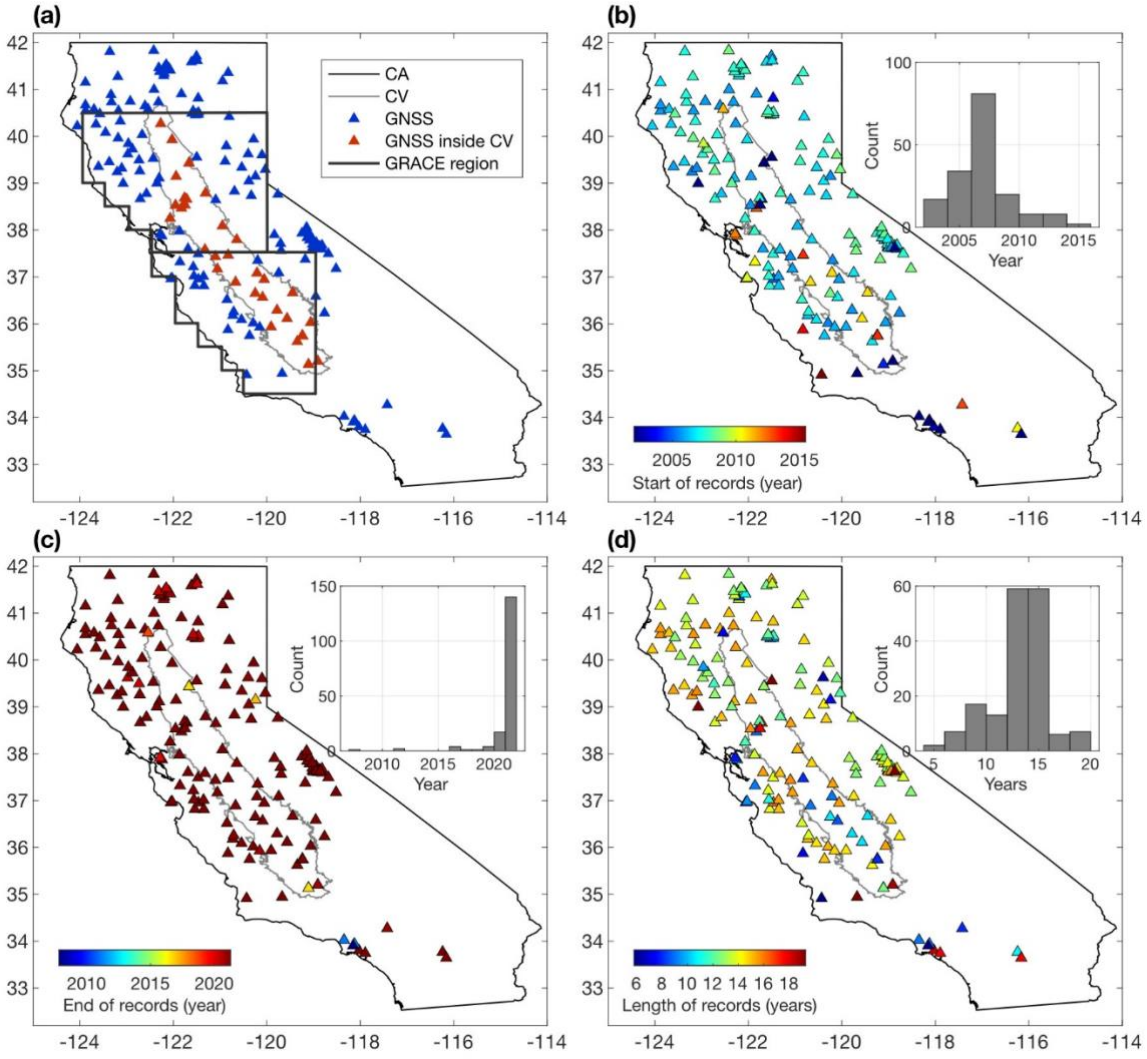

Figure S5. Overview of GNSS data availability. (a) Location of GNSS sites (same as Fig. 1b), (b) start year of GNSS time series, (c) end year of GNSS time series, and (d) length of GNSS time series in years.

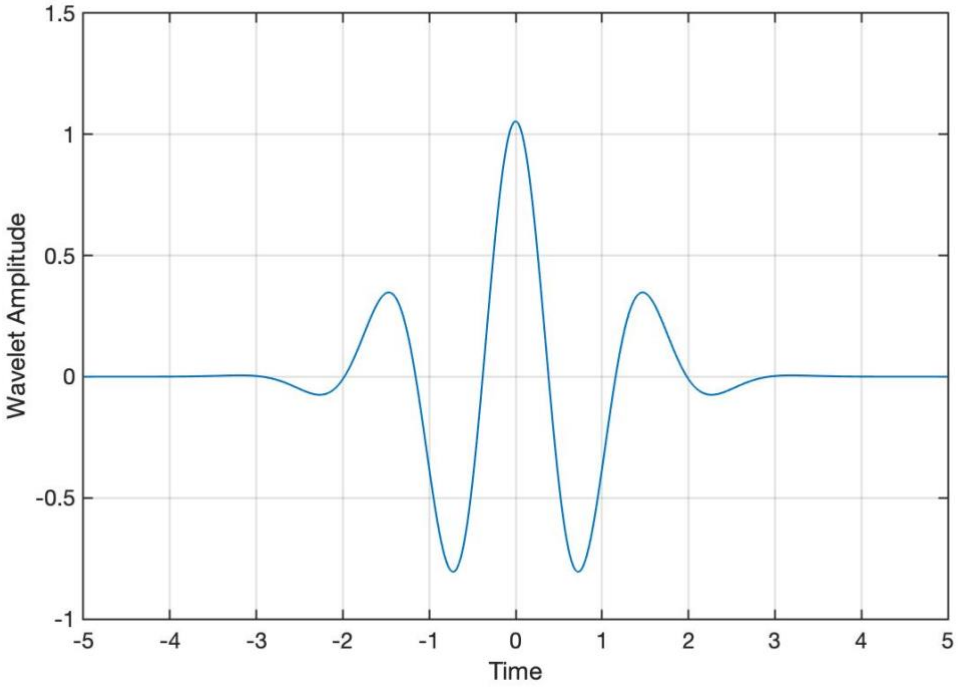

Figure S6. Wavelet Base Function. For the wavelet-based time-frequency analysis in this study, we apply a Derivative of Gaussian (DOG) as a wavelet base function. Shown here is a DOG of 8th order.

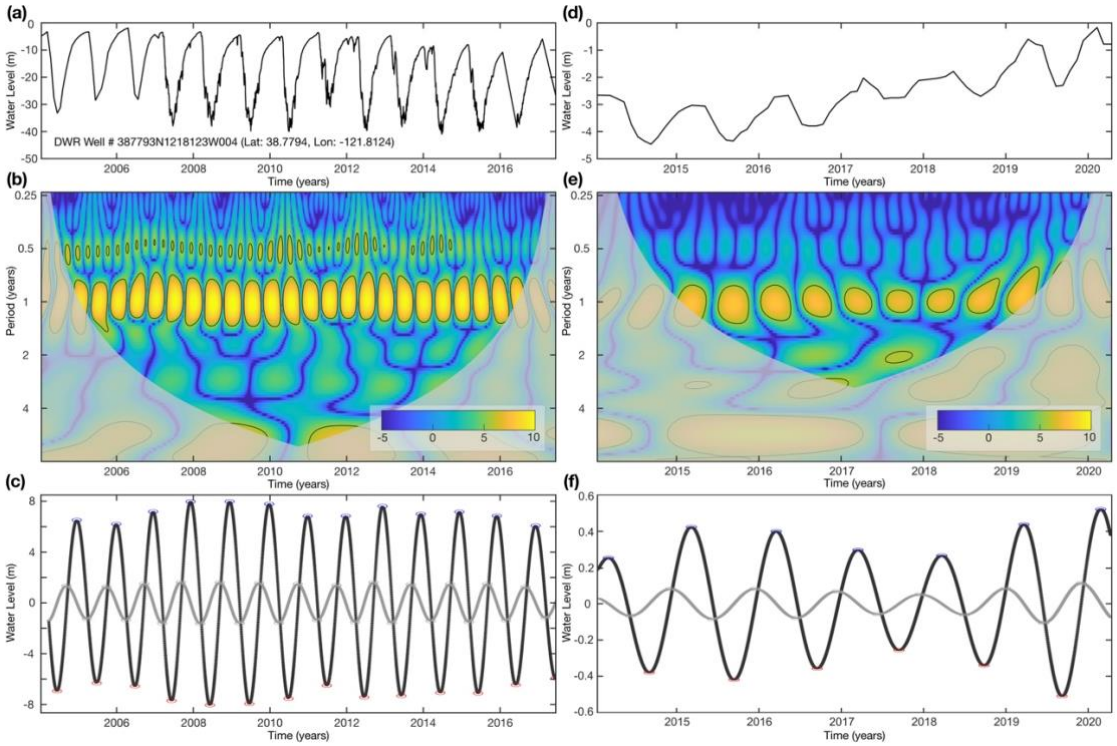

Figure S7. Example for isolating the annual signal component from a time series with wavelet analysis using DOG wavelets (Fig. S6) and for time series with different temporal sampling rates. (a) Example groundwater level time series as measured at the DWR well #387793N1218123W004 with daily temporal resolution and two gaps in 2016 and 2017 which were interpolated to daily sampling rate, (b) corresponding wavelet power spectrum with cone-of-influence (black thick line) and contour line for signal power above signal noise level (black thin lines), and (c) the determined seasonal signal component (black line) reconstructed from signal power exhibited at the period range of 0.75-1.25 years. (d-e) Same as a-c but for a groundwater level time series with monthly temporal resolution, here, as measured at the DWR well #387626N1213651W002. Blue and red ellipses identify annual maxima and minima. The gray line is the temporal derivative of the reconstructed annual signal, with maxima and minima indicating maximum increase or decrease in the annual signal. Data gaps longer than three months in the original time series are masked out in the reconstruction. Here, gaps in 2016 and 2017 are shorter and do not affect the seasonal signal's isolation.

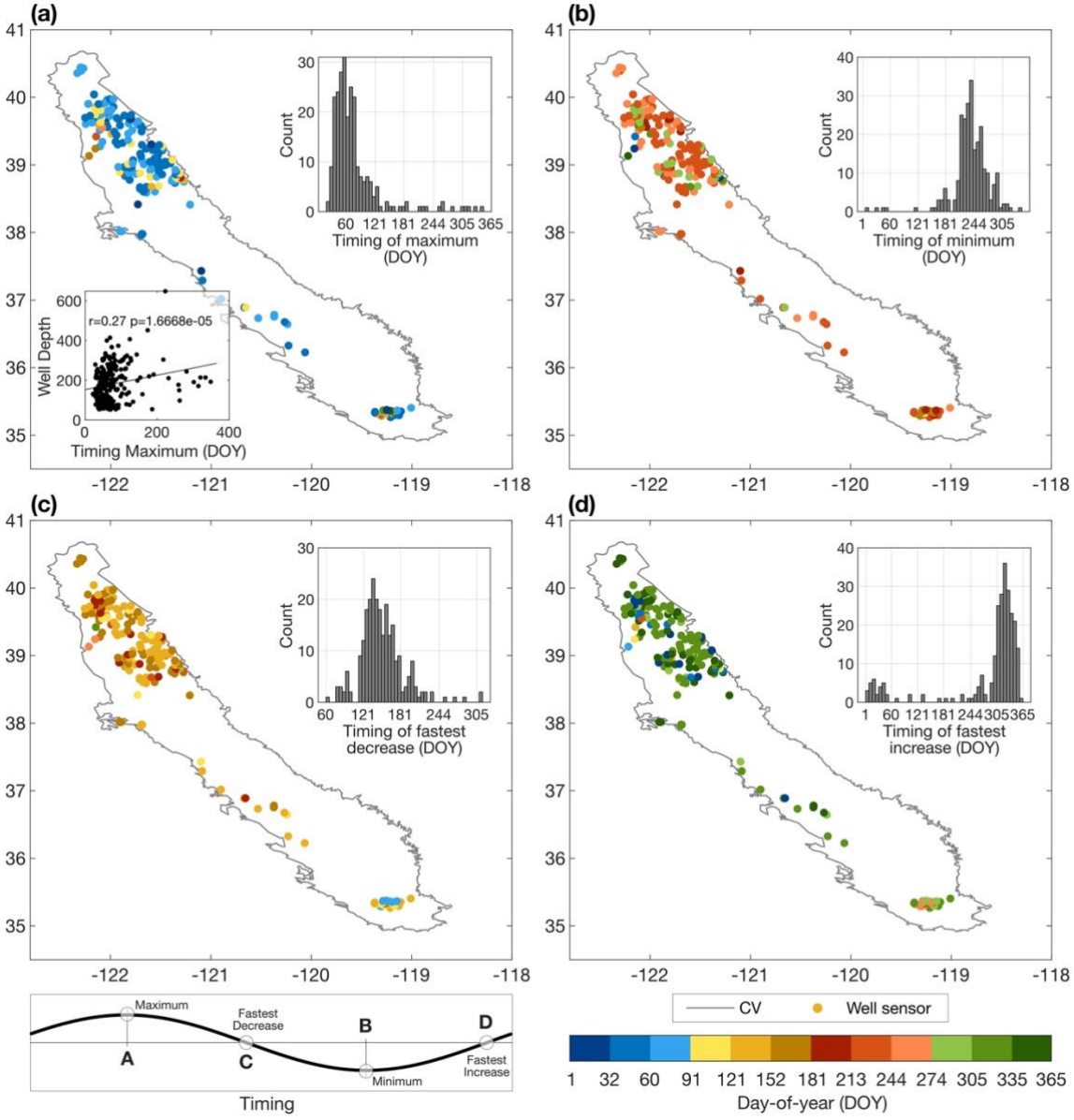

100

Figure S8. Timing of annual groundwater level variations (median DOY of peak time during respective observation period). Timing of extremes in annual groundwater level variations at deepest sensor with depth of below 50 m throughout the Central Valley, and corresponding histogram, for (a) maximum groundwater level occurring during winter, (b) minimum groundwater level during summer, (c) fastest groundwater level decrease during spring, and (d) fastest groundwater level increase during fall.

105

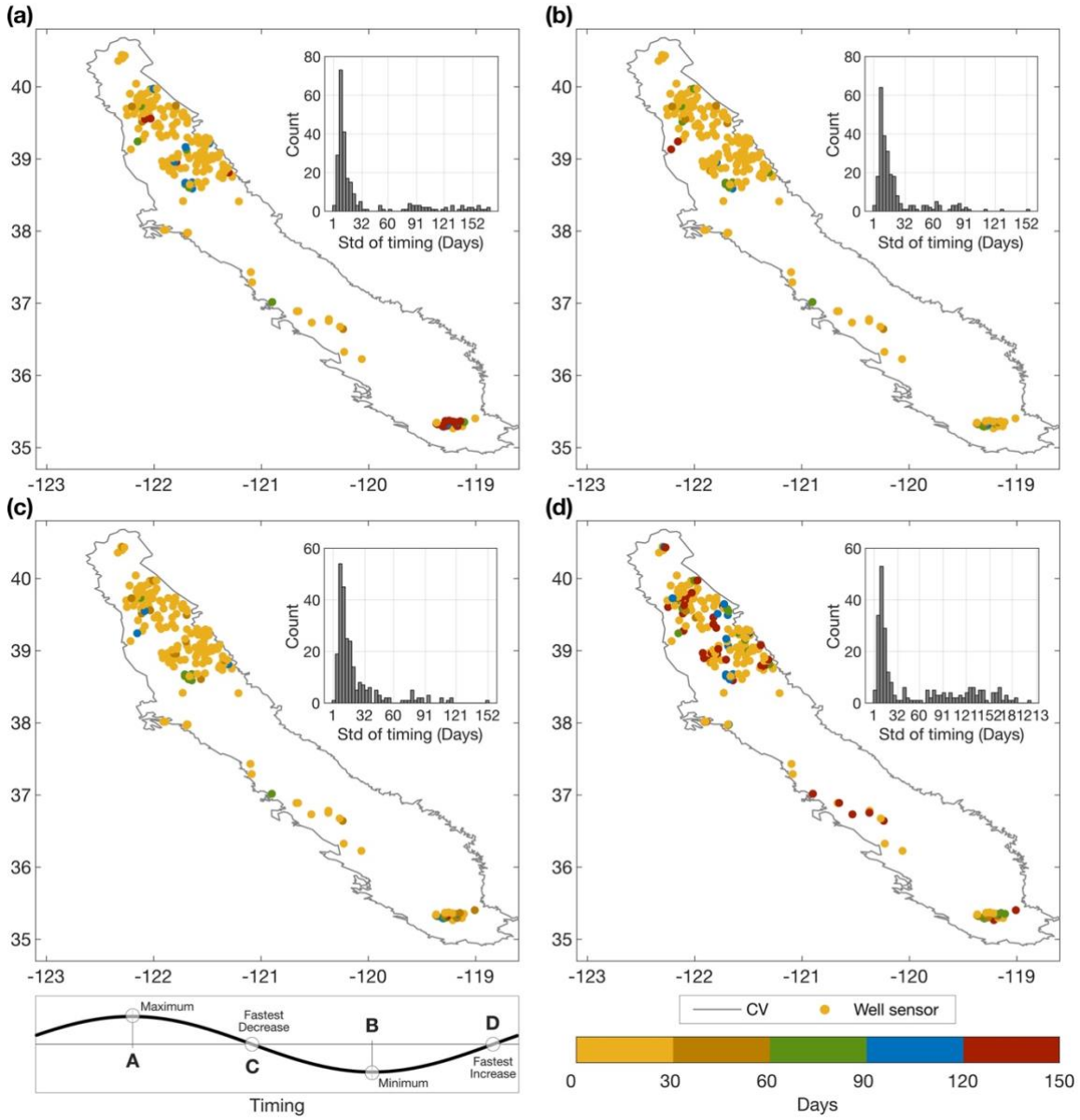

Figure S9. Standard deviation of timing of annual groundwater level variations. Standard deviation (std) of the year-to-year timing of seasonal variations in available groundwater records from observation wells shown in Fig. S8, and corresponding histogram, for (a) maximum groundwater level, (b) minimum groundwater level, (c) fastest groundwater level decrease, and (d) fastest groundwater level increase. A small standard deviation indicates very regular timing of the oscillation between maximum and minimum groundwater level each year, during the years on record.

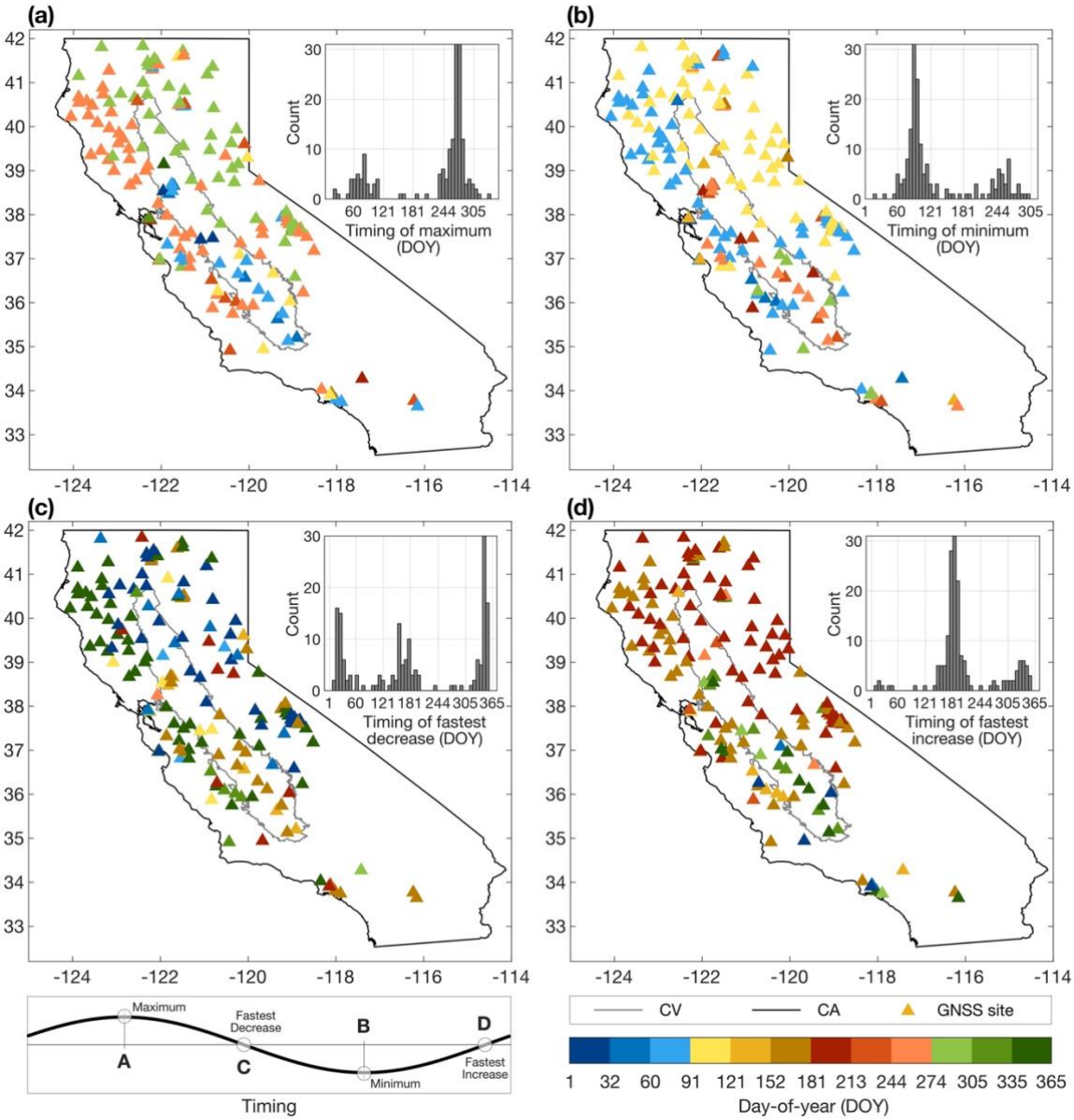

Figure 10. Timing of annual vertical land motion (VLM). Timing of extremes in annual VLM at GNSS sites throughout California, and corresponding histogram, for (a) maximum VLM, (b) minimum VLM, (c) fastest decrease of VLM, and (d) fastest increase of VLM.

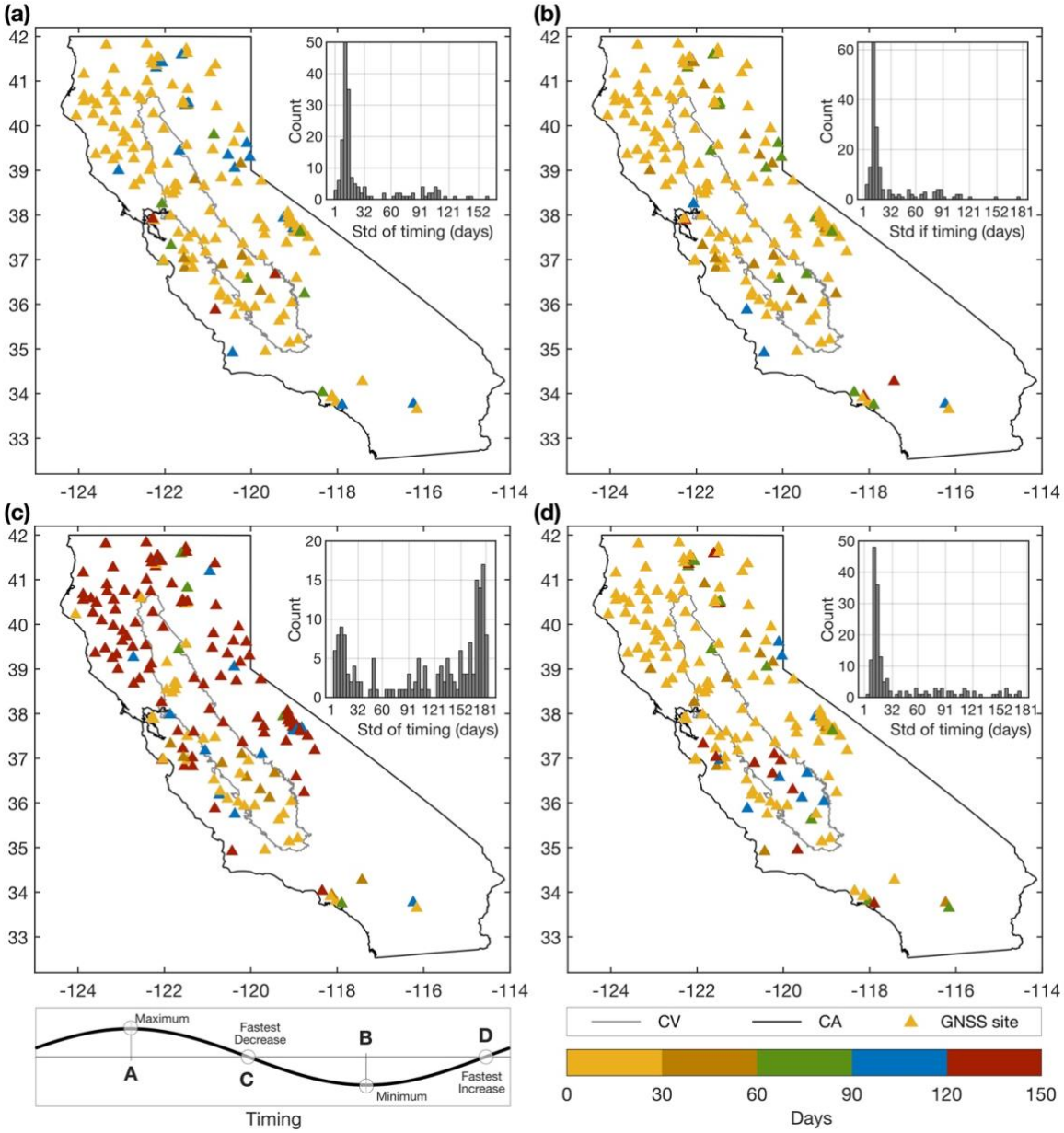

Figure S11. Standard deviation of timing of annual vertical land motion. Standard deviation (std) of the year-to-year timing of seasonal variations in vertical land motion at GNSS sites shown in Fig. S10, and corresponding histogram, for (a) maximum VLM, (b) minimum VLM, (c) fastest VLM decrease, and (d) fastest VLM increase. A small standard deviation indicates very regular annual oscillation between uplift and subsidence each year, during the years on record.

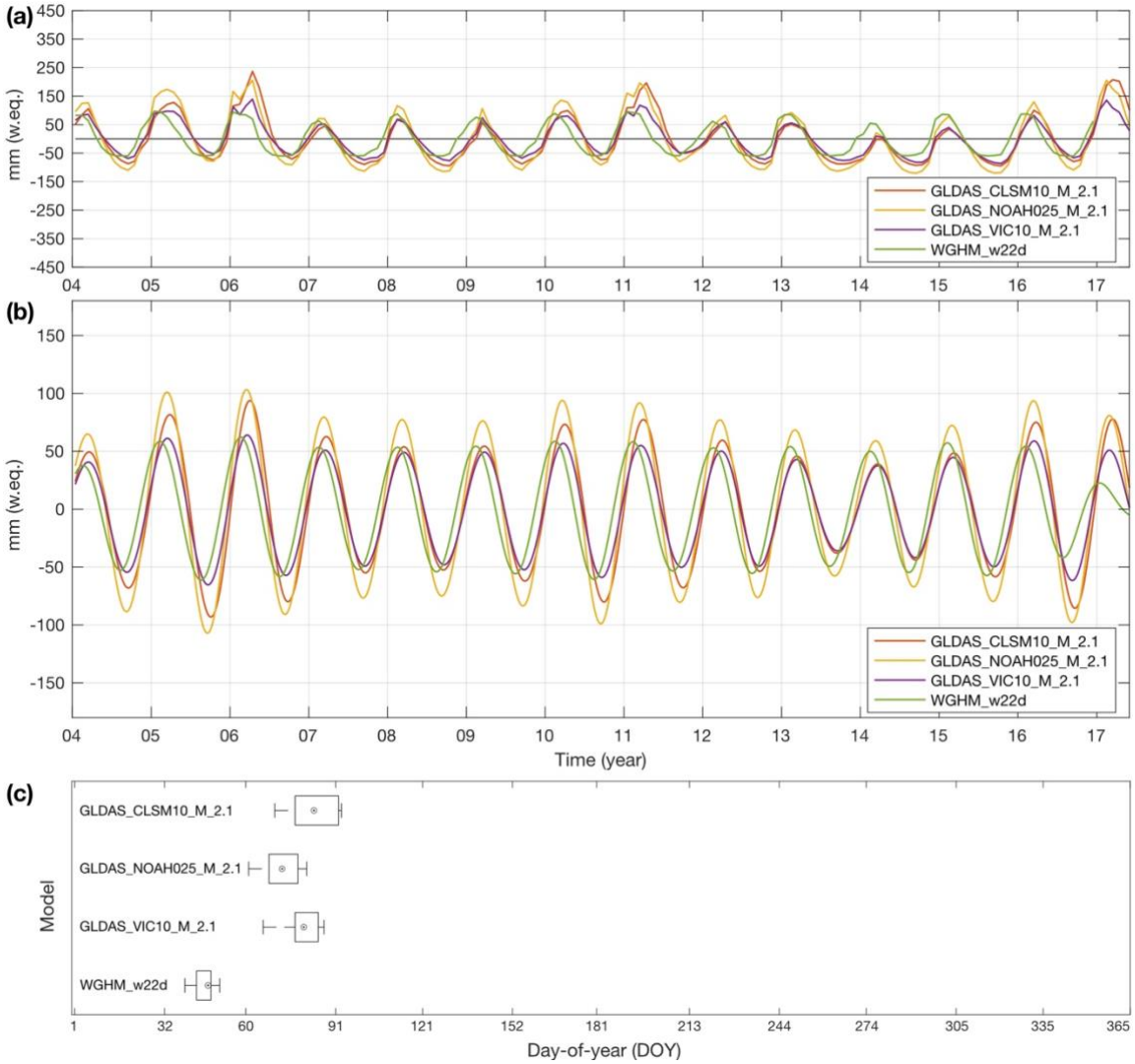

125 **Figure S12. Soil storage variations from different hydrological models. (a) Monthly time series of soil moisture variation from four global hydrological models (GLDAS-CLSM, -NOAH, -VIC and WGHM), (b) corresponding reconstructed annual signal component after wavelet analysis at daily sampling resolution, and (c) timing of the maximum of the annual signal in day-of-year (DOY).**

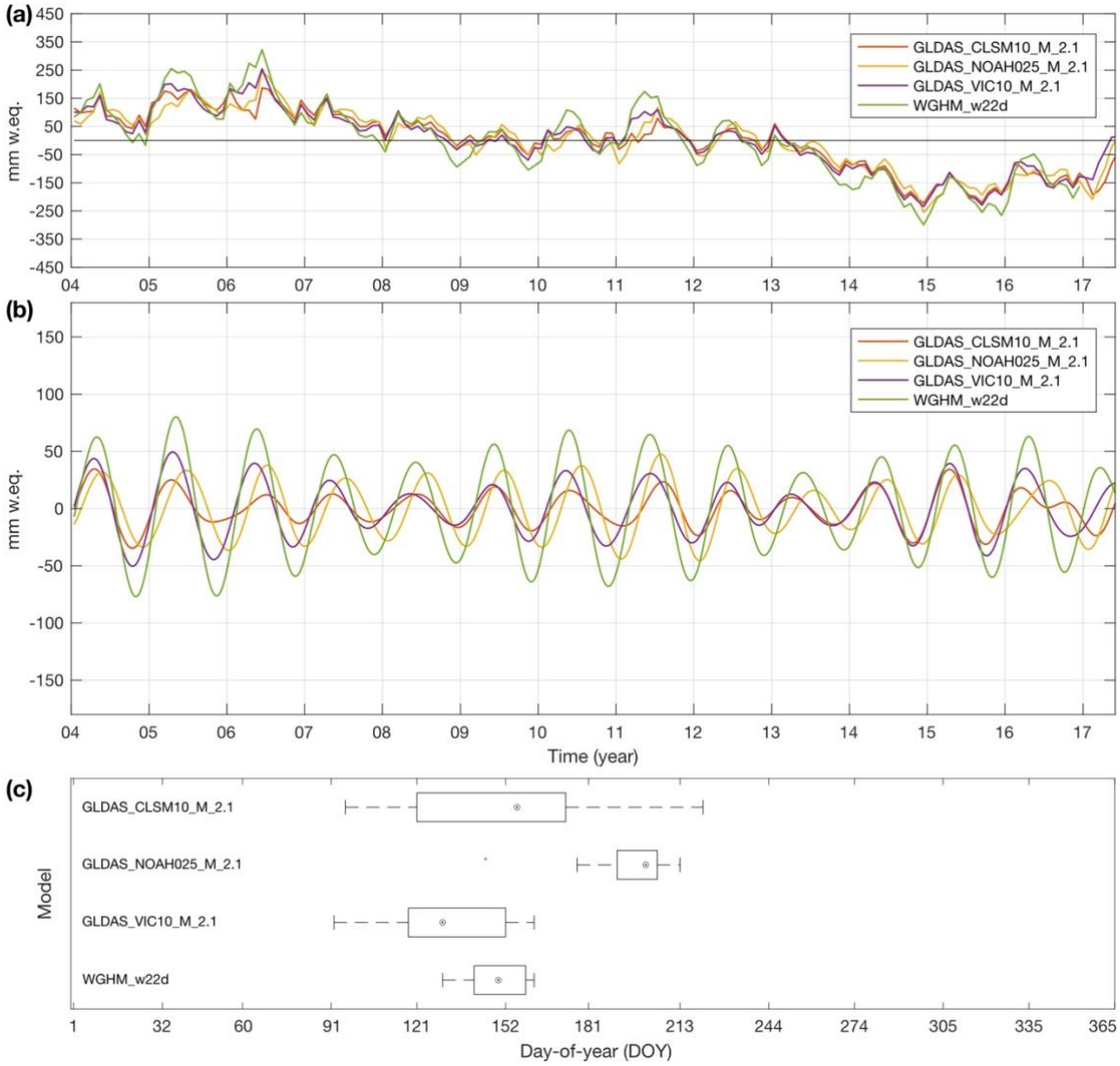

Figure S13. Groundwater storage variations from different hydrological models. (a) Monthly time series of groundwater storage variations calculated from four different global hydrological models (GLDAS-CLSM, -NOAH, -VIC and WGHM) (shown in Fig. S12) and further hydrology (variations in total, surface and snow water as shown in Fig. 1c), (b) corresponding reconstructed annual signal component after wavelet analysis at daily sampling-resolution, and (c) timing of the maximum of the annual signal in day of year.

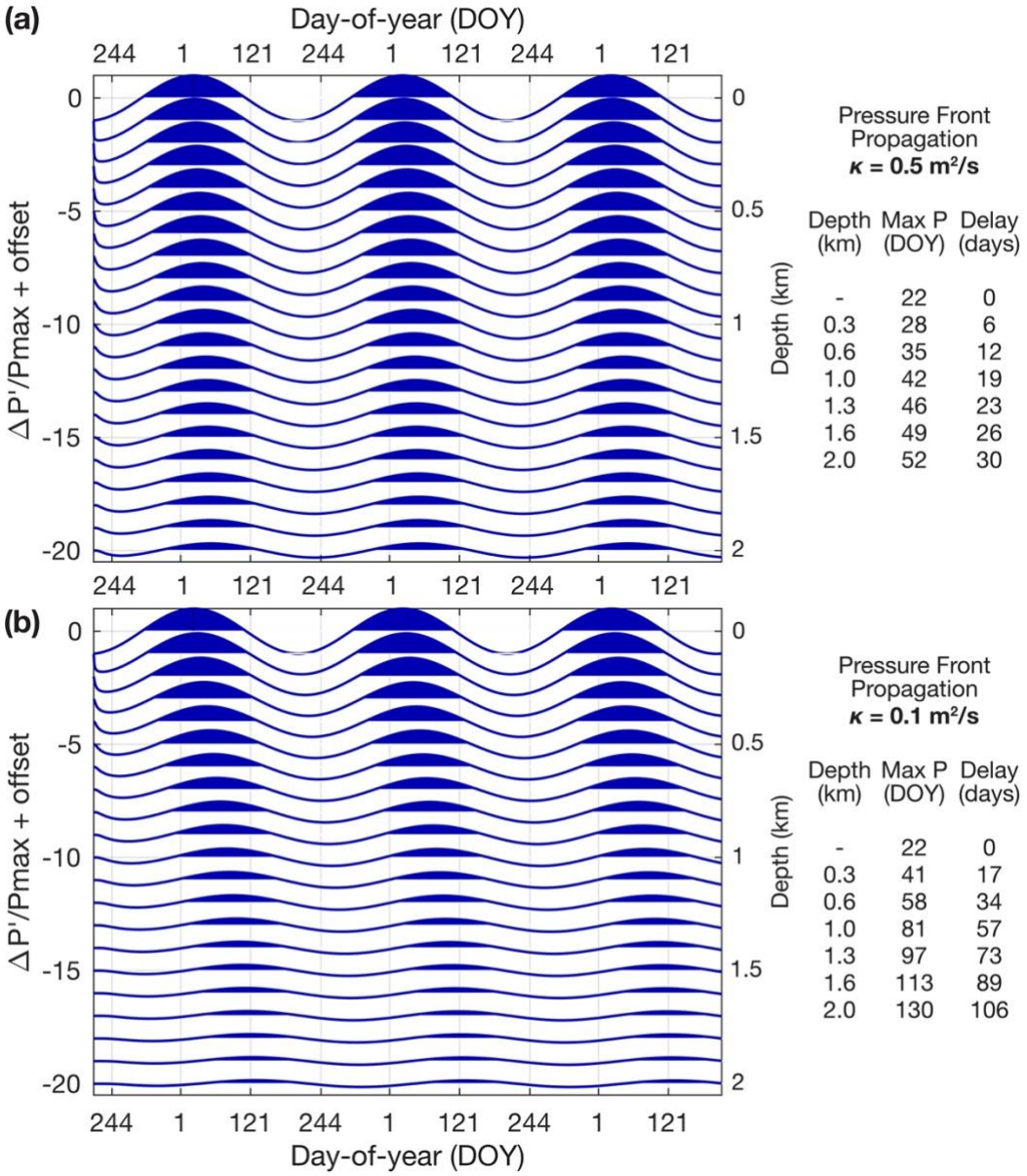

Figure S14. Pressure front propagation for different hydraulic diffusivities. Normalized pressure change ($\Delta P'/P_{max}$) at different depth due to standard 1D calculation of pressure front propagation along mountain block recharge conduits in the fractured bedrock of the Sierra Nevada Mountains. Same as Figure 7, but for hydraulic diffusivity (a) κ = 0.5 m2/s, (b) κ = 0.1 m2/s. Graphs are incrementally offset by -1 for each depth. In upper groundwater layers of the Sierra Nevada, maximum pressure occurs on January 22nd (DOY 22), which is driven by mean annual water availability in the area (Fig. 6b). Table to the right indicates DOY and time delay of the pressure propagation to depth of 300-2000 m.

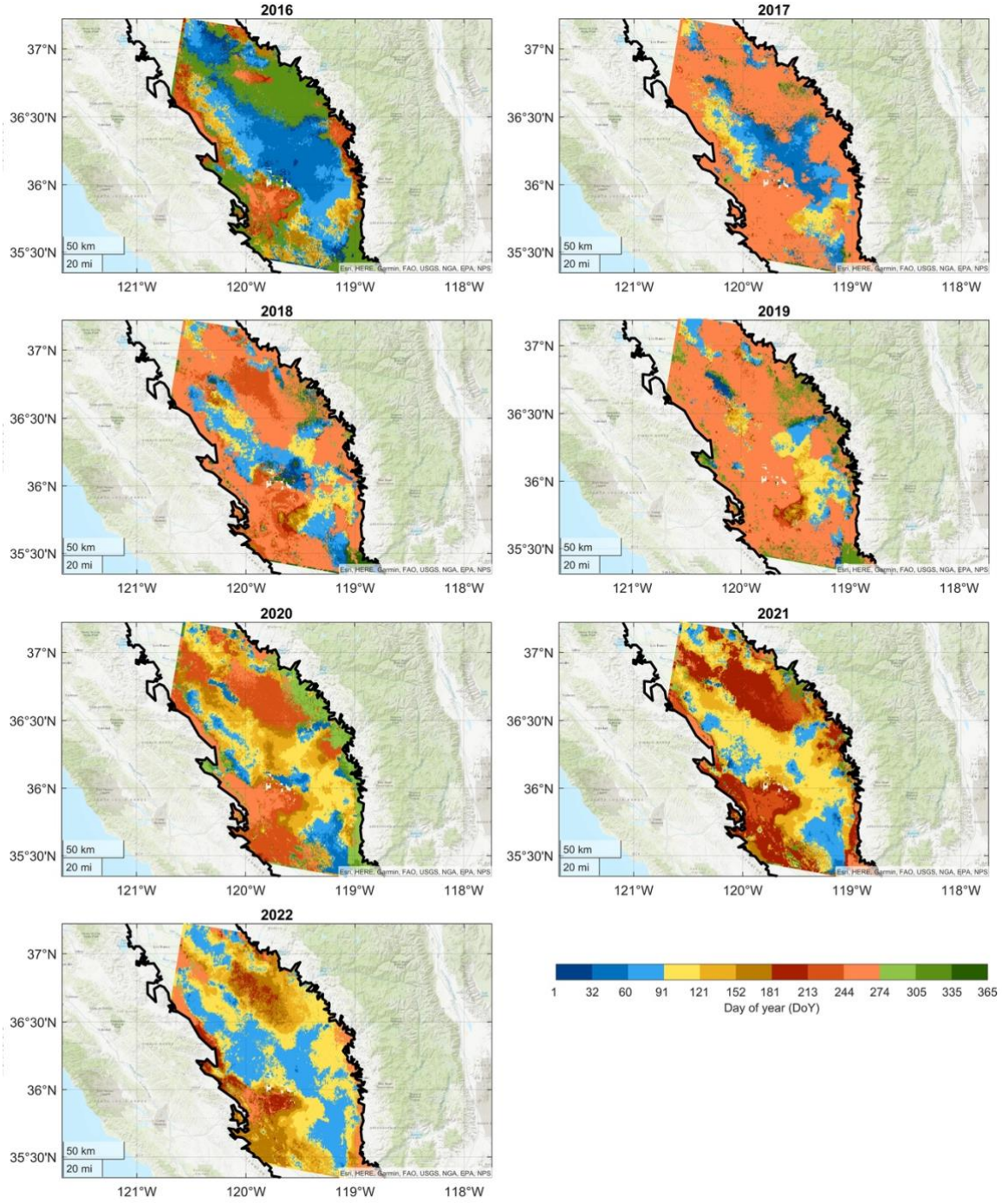

Figure S15. Yearly annual phase (median DOY of peak LOS) of InSAR deformation time series for years of 2016-2022.

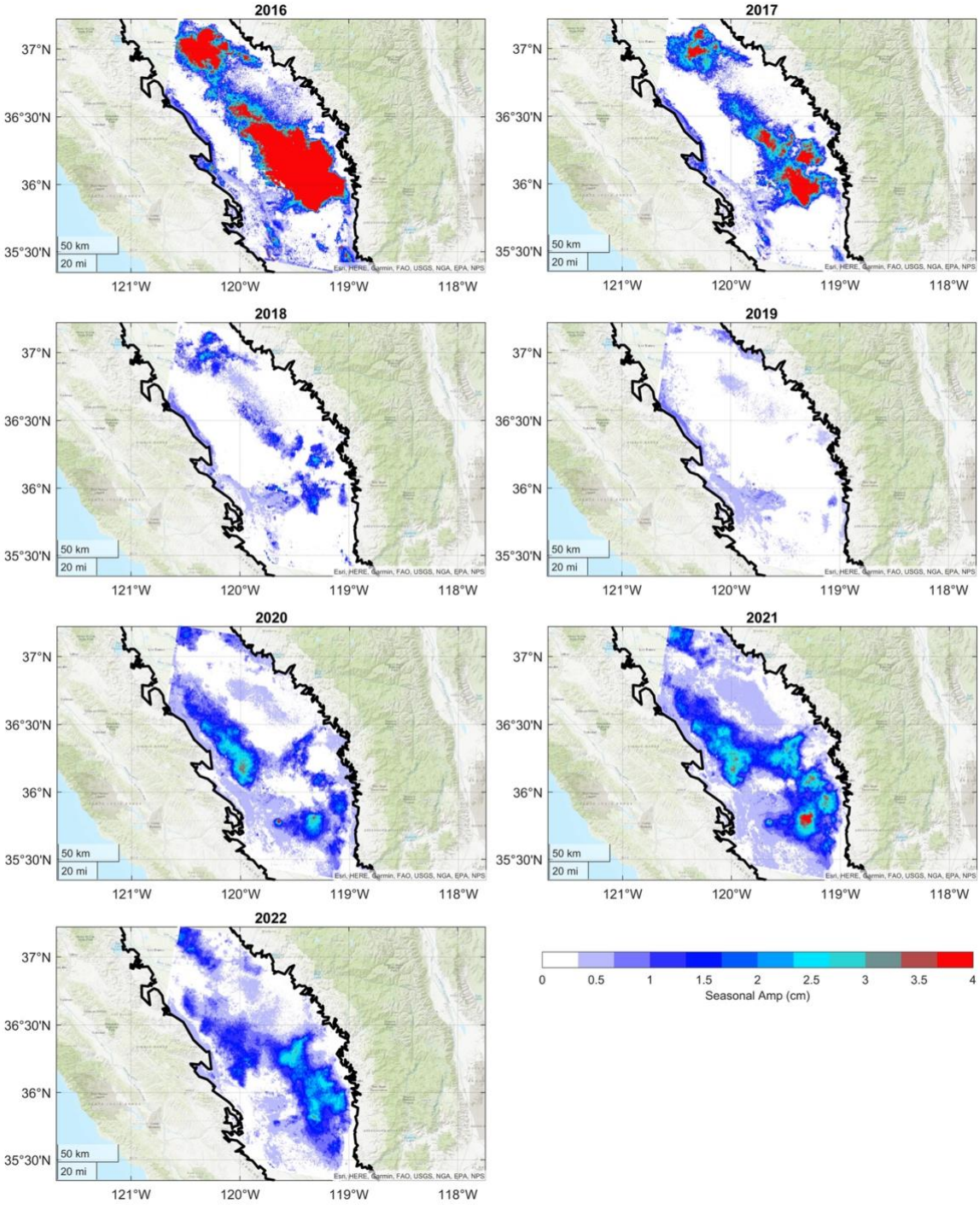

Figure S16. Yearly annual amplitude of InSAR deformation time series for years of 2016-2022.